Sub-Micrometer-Scale Mapping of Magnetite Crystals and Sulfur Globules in Magnetotactic Bacteria Using Confocal Raman Micro-Spectrometry

Stephan H. K. Eder[1], Alexander M. Gigler[1,2], Marianne Hanzlik[3], Michael Winklhofer[1]*

1 Department of Earth and Environmental Sciences, Ludwig-Maximilians-University Munich, Munich, Germany, 2 Center for NanoScience (CeNS), Munich, Germany, 3 Department of Chemistry, Elektronenmikroskopie, Technical University Munich, Munich, Germany

Abstract

The ferrimagnetic mineral magnetite Fe_3O_4 is biomineralized by magnetotactic microorganisms and a diverse range of animals. Here we demonstrate that confocal Raman microscopy can be used to visualize chains of magnetite crystals in magnetotactic bacteria, even though magnetite is a poor Raman scatterer and in bacteria occurs in typical grain sizes of only 35–120 nm, well below the diffraction-limited optical resolution. When using long integration times together with low laser power (<0.25 mW) to prevent laser induced damage of magnetite, we can identify and map magnetite by its characteristic Raman spectrum (303, 535, 665 cm^{-1}) against a large autofluorescence background in our natural magnetotactic bacteria samples. While greigite (cubic Fe_3S_4; Raman lines of 253 and 351 cm^{-1}) is often found in the *Deltaproteobacteria* class, it is not present in our samples. In intracellular sulfur globules of *Candidatus* Magnetobacterium bavaricum (*Nitrospirae*), we identified the sole presence of cyclo-octasulfur (S_8: 151, 219, 467 cm^{-1}), using green (532 nm), red (638 nm) and near-infrared excitation (785 nm). The Raman-spectra of phosphorous-rich intracellular accumulations point to orthophosphate in magnetic vibrios and to polyphosphate in magnetic cocci. Under green excitation, the cell envelopes are dominated by the resonant Raman lines of the heme cofactor of the b or c-type cytochrome, which can be used as a strong marker for label-free live-cell imaging of bacterial cytoplasmic membranes, as well as an indicator for the redox state.

Data Availability: The authors confirm that all data underlying the findings are fully available without restriction. All relevant data are within the paper.

Competing Interests: The authors have declared that no competing interests exist.

* Email: michael@geophysik.uni-muenchen.de

Introduction

The ferrimagnetic mineral magnetite (stoichiometric formula: Fe_3O_4) is found as biomineralization product in magnetotactic microorganisms such as bacteria [1], algae [2], protozoans [3], and a diverse range of animals, e.g., molluscs [4], teleost fish [5,6] and birds [7,8]. In magnetotactic microorganisms, typically a dozen of intracellular magnetite crystals, the magnetosomes, with 35–120 nm particle size each, are arranged in the form of one or several magnetosome chains, imparting a magnetic dipole moment to the cell body (for recent reviews, see [9–11]). The chains are mechanically linked to the cytoplasmic membrane, so that the magnetic torque due to an external magnetic field acting on the chain can be directly transmitted to the cell body, thereby aligning the swimming cell with the external magnetic field. The advantage of swimming along magnetic field lines, a behavior referred to as magnetotaxis, is not fully understood yet, since key aspects of the ecology and metabolism of these microorganisms remain to be elucidated. Similarly, the role of magnetite in animals is only partly understood. It is likely to be involved in mediating a magnetic sense in animals, at least in salmon and homing pigeons, because magnetite found in various nerve tissues of these animals occurs in the magnetic single domain grain size range [5–7] just like in magnetic bacteria. In contrast, magnetite in chiton teeth serves as hardening agent [4] and occurs in particles sizes of ~ 200 nm, above the single domain threshold size [12]. The origin and role of nanoparticulate magnetite (<10 nm) in the pigeon beak [8] and in pathological human brain tissue [13,14] is unknown.

Since biomineralized magnetite always occurs in grain sizes well below the optical diffraction limit, conventional transmission electron microscopy (TEM) combined with selected-area electron diffraction is the usual method of choice for detection and imaging of intracellular magnetite. Advanced TEM techniques such as off-axis electron holography can be used to gain additional information on the magnetic microstructure of magnetosome chains [15]. With the advent of X-ray zone-plate lenses that limit X-ray spot sizes down to few tens of nm, scanning transmission X-ray microscopy (STXM) allows one to visualize bacterial magnetosome chains and map the magnetic polarity along the chain [16–18], albeit at a coarser resolution compared to electron holography. Yet, as a synchrotron-based method, STXM is far from becoming a routine technique. The magnetic dipole pattern

due to a magnetosome chain can also be visualized with magnetic force microscopy [19–22] and with near-field scanning optical microscopy [23] provided that the chain is close to the surface of the sample, which should be sufficiently smooth to avoid topographic artifacts. Recently, the magnetic stray field distributions due to magnetosome chains were mapped with a resolution of 400 nm using optically detected magnetic resonance [24].

Here we demonstrate that confocal Raman spectroscopy is an effective tool for detecting and mapping intracellular magnetite crystals with grain sizes of typically 100 nm, well below the optical resolution limit. In essence, the effective resolution is enhanced by first acquiring Raman spectra on a grid with mesh width 100 nm and then by filtering the spectra for the specific Raman lines of magnetite. Confocal Raman microscopy has been used to detect biomineralized magnetite in situ [25,26], but to our knowledge not for mapping the intracellular distribution of magnetite. Confocal laser scanning microscopy in reflectance mode [27] or transmission mode [28] has been applied to image chains of magnetosomes, but relies on additional analytical techniques to determine the chemical composition of the material. Compositional information is important because magnetosomes in the *Deltaproteobacteria* can also be made of the ferrimagnetic sulfospinel greigite (Fe_3S_4) [29–38], which compared to magnetite has a 50 % lower saturation magnetization but a higher anisotropy field, which helps stabilize the magnetization of greigite magnetosomes against thermal fluctuations [39].

For Raman-based compositional mapping, we here selected two types of uncultured magnetic bacteria that contain magnetite crystals with typical length dimension 100 nm, *Candidatus* Magnetobacterium bavaricum (MBav, Figure 1A) and uncultured magnetic vibrios (Figure 1B). From magnetotactic cocci (Figure 1C) we later recorded Raman spot-measurements for comparison. All the bacteria were extracted from sediments of lake Chiemsee in Bavaria (Southern Germany) [40]. In the vibrios, the magnetite crystals are arranged in the form of a single-strand magnetosome chain consisting of 10 to 20 crystals of regular morphology with prismatic habit (see Figure 1A), a trait that is only known in magnetic bacteria from the *Alphaproteobacteria* and a single member (strain SS-5) from the *Gammaproteobacteria*, but not from *Deltaproteobacteria* and *Nitrospirae* [41,42]. In contrast, the large, rod-shaped cells of MBav (Figure 1A) contain up to 1000 magnetite crystals of claw-shaped habit (typical size of 40 nm thick and 100 nm long), arranged in multi-strand bundles of chains along the axis of the cell body [40,43–48]. MBav with its peculiar chain configuration and phylogenetic affiliation to the *Nitrospirae* phylum was long considered an exotic representative of the group of magnetic bacteria, but meanwhile magnetotactic bacteria of the *Nitrospirae* phylum with chain architectures similar to those in MBav have been reported worldwide [49–51].
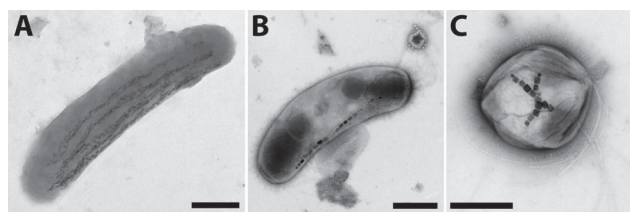

Figure 1. Transmission electron micrographs of three different morphotypes of magnetotactic bacteria extracted from lake sediments. (A) *Candidatus* Magnetobacterium bavaricum (MBav), **(B)** magnetotactic vibrio, and **(C)** magnetotactic coccus. (scale-bars are 1 μm).
doi:10.1371/journal.pone.0107356.g001

Apart from magnetosome chains, other intracellular accumulations of inorganic compounds in magnetic bacteria may be phosphorous containing granules and/or sulfur globules [52]. Bacteria in general accumulate inorganic phosphorous-compounds in the form of ortho-, poly- or pyrophosphate in intracellular granules [53]. At least three different forms of sulfur — i.e., polysulfanes, cyclo-octasulfur S_8, and polythionates — have been suggested to be present in bacterial sulfur globules using X-ray near-edge absorption spectroscopy (XAS) [54–57] or Raman spectroscopy [58,59]. However, as pointed out by George et al. [57], earlier XAS-based evidence of polymeric sulfur in sulfur bacteria may well have been an experimental artifact. S_8 so far has only been identified in the *Proteobacteria* [60], but to our knowledge not in the *Nitrospirae* phylum. In MBav, elemental sulfur has been suggested to be the main constituent of sulfur globules based on their solubility in methanol [44], but the exact allotrope remains unknown. Using the Raman reference spectra of sulfur allotropes compiled by Eckert and Steudel [61], we will here determine the nature of the sulfur allotrope in MBav.

Results

In our sample of magnetotactic bacteria (Figure 2) five typical Raman spectra were picked from single voxels in Mbav and vibrio cells (Figure 3A and B). While the background in the single-voxel spectra is dominated by autofluorescence from organic compounds, one can see a number of distinct lines superimposed. When stacking single-voxel spectra (see Methods), the relevant lines become more dominant (Figure 3E-F). The set of three lines at 303, 535, and 665 cm^{-1} corresponds to stoichiometric Fe_3O_4 ([62], c.f. Table 1), while greigite (cubic Fe_3S_4), as often observed in magnetotactic bacteria from the *Deltaproteobacteria* taxon, would produce lines at 253 and 351 cm^{-1} (see Figure 4 and Table 2). Another magnetite line at 193 cm^{-1} which usually is weak [62,63], appears in the spectrum of a coccus (Figure 5A and Table 2), but not in the one of Mbav or vibrio. On the compositional map for magnetite (Figure 2C), one can clearly recognize linear structures of magnetite in all MBav cells and in some vibrio cells (compare Figure 2C feature "a" with Figure 2A). However, magnetite chains cannot be detected in all vibroid cells in this particular focal plane, which we ascribe to the small focal depth in the confocal set up: magnetite chains lying above or below the focal plane would be missed. In contrast, MBav contains between two and five multi-strand-chains of magnetosomes, so that the probability of observing a strand of magnetosomes in the focal plane is higher.

The energy dispersive X-ray (EDX) spectrum of the vibroid bacterium shows a pronounced phosphorous peak (at 2.0 keV, see Figure 3C). Phosphorous in bacteria is typically stored in acidocalcisomes in the form of orthophosphate (Pi), pyrophosphate (PPi), or polyphosphate (poly-P) [53] (see Table 3 for their Raman shifts). The characteristic Raman shifts of neither poly-P (~ 700 and ~ 1170 cm^{-1}, [64,65]) nor PPi (1022 cm^{-1} [66]) (~ 1050 cm^{-1} [67,68]) are detectable in the Raman spectrum of the vibroid bacterium (Figure 3A and 3E). However, we can identify a sharp peak at ~ 1080 cm^{-1}, which we assign to the $P = O$ symmetric stretching mode of PO_2 [69,70]. The 874 cm^{-1} line due to symmetric stretching of $P(OH)_2$ is not detectable. Thus, the main constituent of the intracellular phosphorous reservoirs in the vibrios (Figure 2D) appears to be orthophosphate, the most stable phosphate.

A distinct sulfur peak (2.3 keV) is seen in the EDX spectrum of MBav, resulting from intracellular sulfur globules. We can identify the chemical nature of sulfur in these globules from the Raman
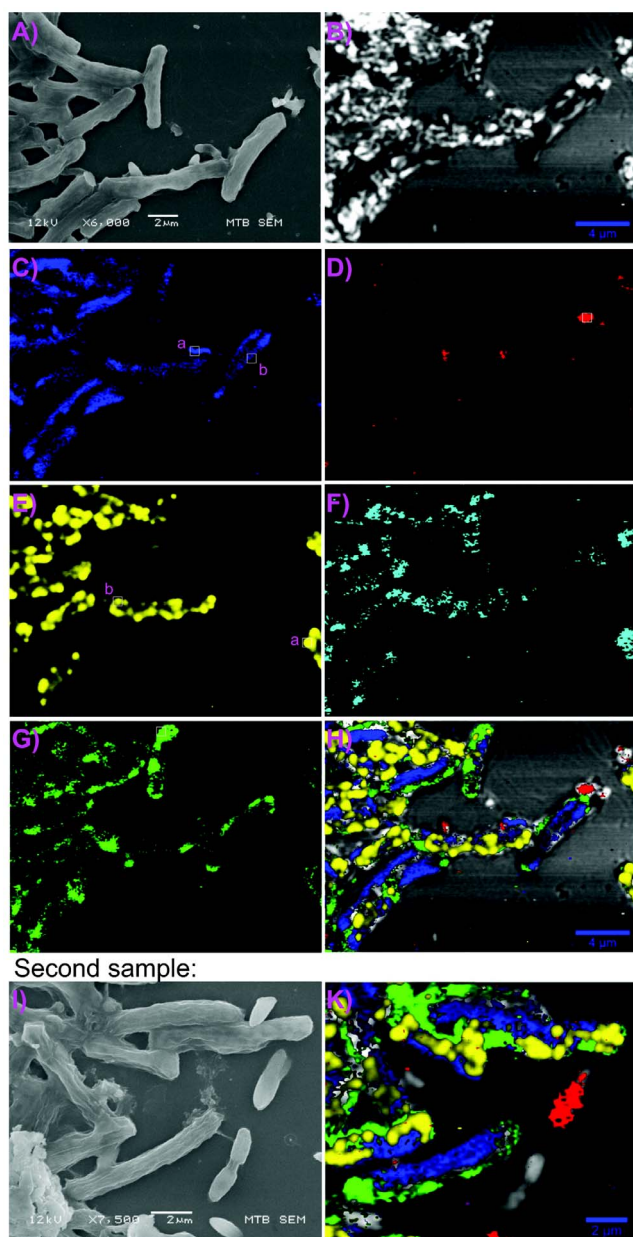
Figure 2. Raman-based compositional mapping of bacteria samples. (532 nm, laser power 0.17 mW) **A)** Scanning-electron micrograph (SEM) showing 6–10 μm long rod-shaped cells of MBav and less elongated (1–3 μm) vibrios. **B)** Confocal reflectance, simulated from scattering intensity at Rayleigh peak. **C)** map of magnetite (303, 535, 665 cm^{-1}), which forms linear structures (magnetosome chains). **D)** map of orthophosphate (1080 cm^{-1}, P-O stretching mode), **E)** map of S_8 (filter: 151, 219. 467 cm^{-1}), which occurs in the form of intracellular globules, **F)** map of 800 to 950 cm^{-1} band, see also Figure 3Bi and 3E upper spectrum. **G)** map of 747 cm^{-1} (cytochrome), closely associated with the plasma membrane, **H)** composite map of B, C, D, E, G. **I)** SEM of another sample, with corresponding composite Raman map shown in **K** (532 nm laser, 0.25 mW, same filters and coloring scheme as in H).
doi:10.1371/journal.pone.0107356.g002

spectrum (Figure 3B), which shows a set of three lines at 151, 219, and 467 cm^{-1} ($\pm$ 2 cm^{-1}). These can be uniquely attributed to elemental oct-atomic sulfur, S_8 (85, 152, 216, 470 cm^{-1}, [71], c.f. Table 4, but note that 85 cm^{-1} is not detectable with our

Rayleigh filter). The two lines at 151 and 219 cm^{-1} represent bending modes characteristic of the S_8-ring. Polymeric sulfur, reported for purple and green sulfur bacteria [55] (however, see [57]) and also suggested to be the form of sulfur in MBav [45], would have lines at 260, 275, 425, and 460 cm^{-1} (see [61] and Table 4), which however were not detectable in our samples. Characteristic lines of other elemental sulfur allotropes from S_6 to S_{20} (compiled in [61] and Table 4) were not detectable either. The asymmetric line at 467 cm^{-1} represents a merger of S-S stretching modes at different Raman shifts within the 460–480 cm^{-1} band [61]. A small but distinct shoulder occurs at 415 cm^{-1}, corresponding to a stretching mode that is Raman inactive in molecular S_8 [61], but active in orthorhombic sulfur crystals (α–S_8). This suggests that S_8 in MBav occurs in condensed structures rather than in the form of isolated molecules. These structures have poor crystallinity as indicated by the width of the asymmetric 467 cm^{-1} line, which is typical of glassy S_8, while α–S_8 crystals would produce a distinct line at 434 cm^{-1} of medium intensity (see [58] and Table 4). As can be seen on the S_8 map (Figure 2E) some cells of MBav contain up to 20 intracellular S_8 globules of ~ 0.5 μm diameter, whereas other cells do not bear detectable amounts of S_8. Round reflective features in the Rayleigh map (Figure 2B, which simulates confocal reflectance qualitatively) are co-localized with S_8 inclusions, while reflective features with irregular morphology do not correspond to sulfur inclusions but rather to unspecific surface features such as sediment or salt particles.

Besides the Raman active lines of S_8, the MBav spectrum (Figure 3B) shows a number of additional lines in the range 800 to 950 cm^{-1} (Figure 3B, i), which have been reported for crystalline α–S_8 [61] and assigned to combinations of stretching vibrations (two-phonon processes). These are generally much weaker than the characteristic S_8 lines. The assignment of the two-phonon band to crystalline α–S_8 is not unique because some organic groups have vibrational modes in this wavenumber range, too (e.g., [72,73] or in Table 5). Therefore, to find out if the broad band is associated with sulfur at all, we tested for co-localization on the respective compositional maps (Figure 2E and F). We found the broad band to be always associated with S_8 and suggest it is the two-phonon band of sulfur. The intensity of the two-phonon band is significantly weaker than that of S_8.

S_8 has an indirect band gap of 2.61 eV [61], that is, light of wavelenghts $\leq$ 476 nm can be expected to excite resonance Raman scattering. In contrast, the green laser light we used (532 nm, 2.34 eV) should not produce electronic excitations and therefore the S_8 related lines in our Mbav spectra should not be overemphasized due to resonance Raman scattering. To test for resonance effects, we also acquired Raman spectra with yet lower photon energies (red: 638 nm, 1.95 eV; and near infrared/N-IR: 785 nm, 1.58 eV). Figure 6 shows that the three major peaks due to S_8 are similarly expressed under all illuminations, which rules out resonance scattering under the green light condition. Due to the different filters used for blocking the Rayleigh band, the characteristic S_8 line at ~ 90 cm^{-1} is visible under N-IR, but not under shorter wavelength excitation (Figure 6). Also with the N-IR settings, a peak at 120 cm^{-1} becomes apparent, which is not known for elemental sulfur allotropes, but for oxidized magnetite and maghemite, respectively [74].

Last, a number of robust lines (747, 1126, 1312, 1586 cm^{-1}, Figure 3F) are spatially associated with each other and concentrated near the cell envelope (Figure 2G). These lines appear
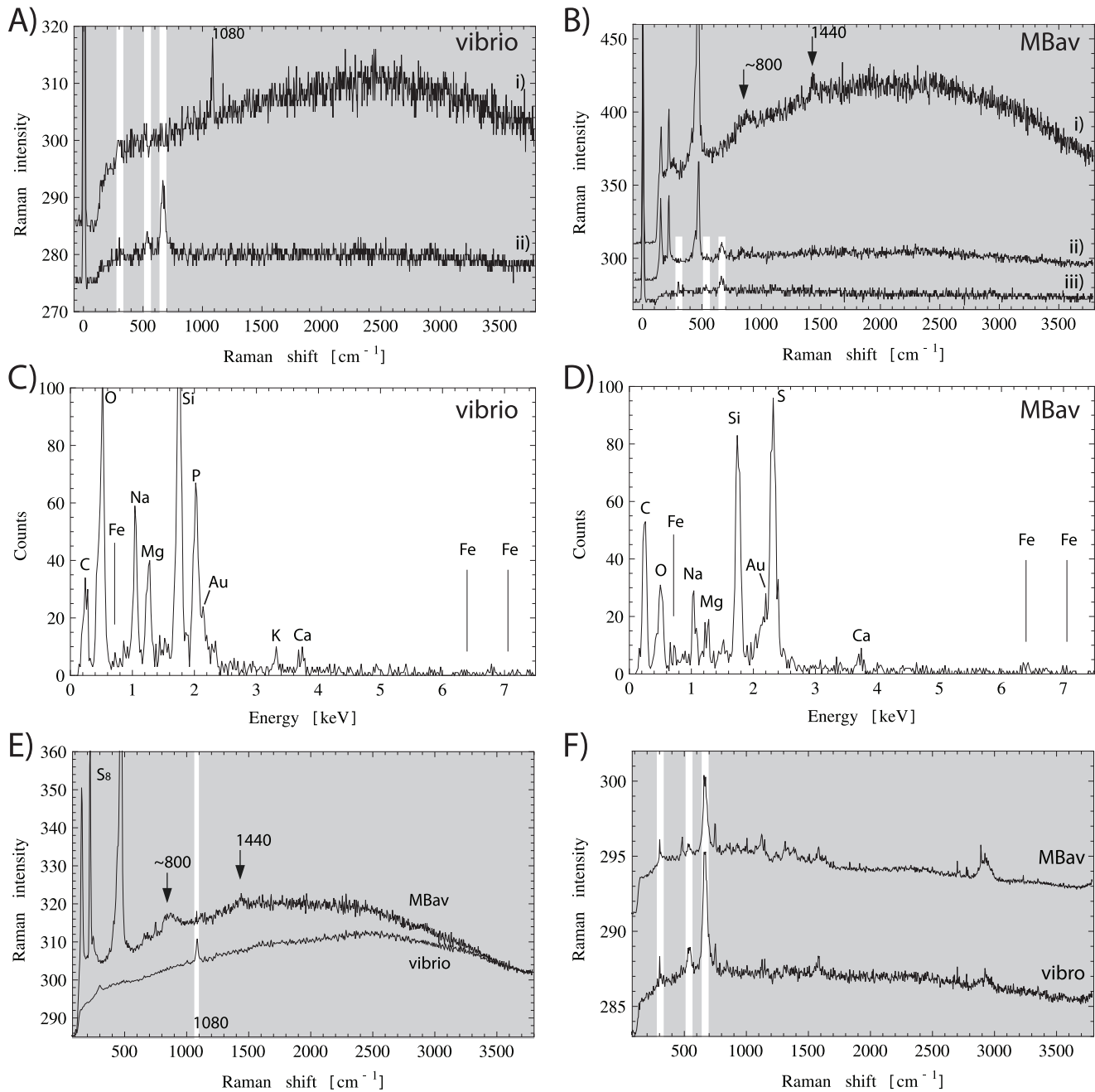
Figure 3. Typical Raman spectra of magnetic bacteria. A-B) recorded at a single-pixel ($\sim$400 nm size), as marked in Figure 2 (white open boxes). **A)** vibrio: (i) intracellular phosphorous reservoir (white box in Figure 2D) with a sharp line at 1080 cm^{-1}, characteristic of orthophosphate. (ii) Magnetosome chain (box $"a"$ in Figure 2C), with the three characteristic lines of magnetite at 303, 535, and 665 cm^{-1} (white bars). **B)** MBav (i) intracellular sulfur globules (box $"a"$ in Figure 2E), dominated by S_8 rings (151, 219, 467 cm^{-1}); arrow shows broad band ($\sim$800 cm^{-1}) assigned to two-phonon peak of S_8. The line at 1440 cm^{-1} is typical of fatty acids. (ii) Magnetite (white bars) in cells containing also sulfur globules (box $"b"$ in Figure 2E). (iii) Magnetite in cells without sulfur globules (box $"b"$ in Figure 2C). **C)** EDX-spectrum of magnetic vibrio, dominated by phosphorous and oxygen. The Si-line is due to the microscope slide, and the Au-line due to the sputtered gold at the surface. **D)** EDX-spectrum of MBav. Sulfur is clearly present, while oxygen is less abundant than in C. **E, F)** Average spectra obtained by averaging over those regions that exclusively produce Raman lines of sulfur in MBav (E, upper graph), of orthophosphate in vibrio (E, lower graph), and of magnetite in MBav (F, upper graph) and in vibrio (F, lower graph).
doi:10.1371/journal.pone.0107356.g003

dominantly also in the single spectrum of an uncultivated magnetotactic coccus (Figure 5B) and are indistinguishable from those reported by Adar [75] (obtained with the same excitation wavelength as here) for reduced cytochrome c, an electron carrier

in the periplasmatic space. This interpretation is consistent with the observation of the cytochrome Raman lines near the cell envelope.

Table 1. Characteristic Raman lines of iron-oxides and iron-sulfides, compiled from literature.

Magnetite (Fe$_3$O$_4$)				Maghemite (γ-Fe$_2$O$_3$)		
[62]	[92]	[91]	[90]	[92]	[91]	[93]
193m	193w			350w	350w	360
306m	**306m**	**310m**	302m	500w	512w	**500**(wide)
		513m			**665s**	
538m	**538m**	**536m**	533m	700w	**730s**	**700**(wide)
668s	**668s**	**667s**	663m		**1330s**	
Hematite (α-Fe$_2$O$_3$)				Greigite (Fe$_3$S$_4$)	Pyrite (FeS$_2$)	
[62]	[92]	[91]	[90]	[92]	[91]	
226m	**225s**	**225m**	225s	139w	351m	
245m	245m			188m	**386s**	
292w	**291–300m**	**291m**	292s	**250m**	**443s**	
299w				**351s**		
411vs	412m	**411m**	408s	**366sh**		
497w	500w					
612m	611w		613m			
659vs	661w	**671s**				
817w	817w					
1049w						
1103w						
(1320vs)	1321vs	1321vs				
	(synthetic)	(rustle rouge)				

Discussion

Magnetite is a poor Raman scatterer, and, because of its broad-band absorption characteristics (black color), it readily undergoes laser-induced transformation to maghemite and eventually to hematite [63]. The risk of oxidative alteration is potentially higher for a high surface-to-volume ratio, which is especially the case for sub-100 nm crystals as those in magnetotactic bacteria. Therefore, it is critical to adjust the laser power and scanning settings such that a good compromise between signal strength and alteration level is obtained. With the laser power adjusted to lowest possible intensity level (170–250 μW), the magnetosomes in our samples of MBav, vibrios, and cocci showed the Raman lines characteristic of magnetite, but not of its oxidation products. Therefore our settings prove adequate for studying the mineralogical nature of intracellular and extracellular nano-particles made of iron-oxides, without damaging or affecting the initial composition.

It is noteworthy that magnetosomes can be detected in the Raman confocal map, even though their particle sizes (35–120 nm) are far below the optical detection limit (horizontal resolution: 0.61·λ NA = 0.36 μm) and hence not resolvable in the reflectance confocal image (derived from the Rayleigh peak). This virtually enhanced resolution is achieved by processing the acquired spectra, where only those Raman lines are selected that are characteristic of magnetite (303, 535, 665 cm^{-1}). This wavelength filter applied to all pixels scanned then acts as a spatial filter for magnetite, which produces the contrast. To take advantage of the enhanced resolution, the step size for scanning needs to be significantly smaller than the optical resolution limit and here was chosen as 0.1 μm. This allows one to locate the position within a resolvable voxel where a specific material occurs with the highest probability. Although the exact shape and size of the related object cannot be reconstructed, one can assume that its horizontal dimensions are below the optical resolution limit. The Raman map (Figure 2C) clearly demonstrates the arrangement of magnetite particles in the form of one or, as in case of MBav, in the form of multiple chains, consistent with the transmission electron micrographs of Hanzlik et al. [45].

The sulfur globules in the compositional map (Figure 2E) appear as round intracellular structures in MBav. It was known before that MBav accumulates sulfur in intracellular globules, presumably for energy storage [44,47,48], but not in what chemical form. Here, we have shown that the enriched sulfur species is elemental sulfur in an S$_8$-ring configuration. The two-phonon effect is co-localized with the sulfur globules (see map 2E and 2F), which indicates strong interactions between the atoms of different S$_8$-rings. This suggests a dense accumulation of S$_8$-rings. Therefore, it is unlikely that material other than S$_8$ resides in the globules, which is why they can be considered as pure sulfur storages. The cells can use sulfur from these storages to gain energy by oxidation to sulfate (which requires swimming upward from the anoxic sediment where sulfur is collected). Thus, as suggested by Jogler et al. [47], the presence or absence of stored sulfur in individual MBav could quantitatively indicate the energy reserves of the cell (some individual cells of MBav contain S$_8$, others do not; see Figure 2E).

The source of sulfur for the sulfur globules in MBav is not known yet because MBav is not available in culture. In most bacteria with sulfur inclusions, the sulfur substrate is H$_2$S or thiosulfate [60]. Cells of cultivated marine magnetotactic bacteria from the *Alphaproteobacteria* group produce sulfur globules when H$_2$S is added to the growth medium (e.g. [76]). For MBav, which
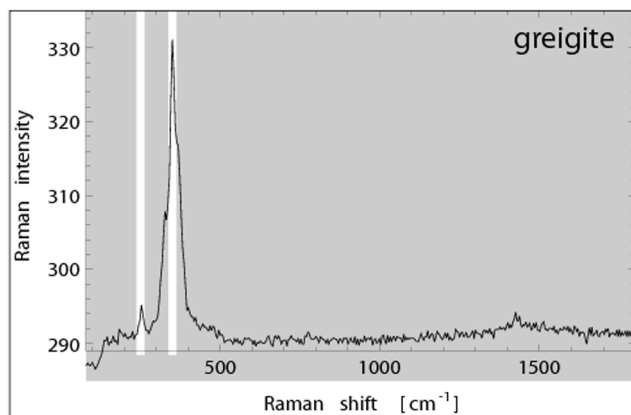
Figure 4. Raman spectrum of a single crystal of greigite (∼10 μm grain size). The band at 351 cm^{-1} has a satellite at 327 cm^{-1} and a shoulder at 367 cm^{-1}. Another line is located at 253 cm^{-1}. Note the absence of lines at wavenumbers> 500 cm^{-1}, particularly in the 660–670 cm^{-1} range, where magnetite and hematite are active. The 190 cm^{-1} line is just not detectable. The spectrum is consistent with observations from literature (c.f. Table 2 and [96]).
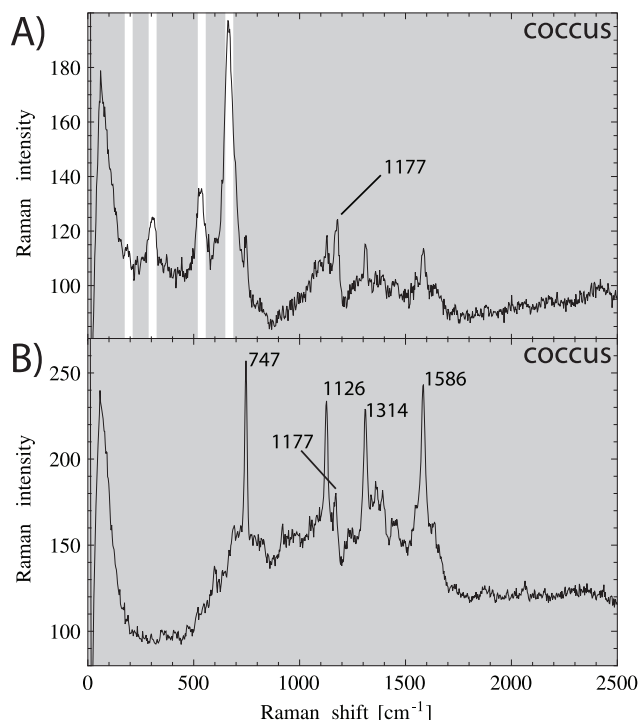doi:10.1371/journal.pone.0107356.g004

Figure 5. Single Raman spectra of a magnetotactic coccus, taken at two different spots with otherwise identical settings. A) Well expressed magnetite lines at 190, 303, 535, 665 cm^{-1} (white bars). **B)** lines of heme group (most likely of reduced cytochrome c) at 747, 1126, 1314, 1586 cm^{-1}. The line 1177 cm^{-1} is present in A) and B) similarly strong, and therefore is not assigned to the heme group, but to polyphosphate (Table 2).
doi:10.1371/journal.pone.0107356.g005

is a freshwater bacterium, Spring et al. [44] proposed H$_2$S as a substrate, but did not detect sulfide (detection limit 0.01 mM) in the depth zone where cells of MBav occurred. Although small amounts of sulfide cannot be ruled out in these microcosms, the sulfur source of MBav could also be thiosulfate, because MBav was found to have a RuBisCO-like protein that in a green sulfur bacterium is involved in some aspect of thiosulfate oxidation [47]. Otherwise RuBisCO could be involved in autotrophic CO$_2$ fixation [76].

The co-occurrence of elemental sulfur and magnetite within individual cells of MBav is surprising from the point of view of inorganic equilibrium chemistry, because the stability fields of the two minerals are separated from each other by the stability field of an iron sulfide mineral such as FeS$_2$ (pyrite) (see figure 7.19 of [77]) or some FeS phase (see [78]). The magnetite and sulfur signals (Maps C and E in Figure 2) are often found to co-occur in the same voxel analyzed, but the compounds are enclosed in membrane vesicles each [47] and therefore are spatially separated, which makes chemical reactions between these unlikely to happen. The co-occurrence of elemental sulfur and magnetite within a cell has also been reported in magnetotactic bacteria from the *Alphaproteobacteria* group (e.g. [57]), which keep growing magnetite even when H$_2$S is added to the growth medium (e.g., [76]). In contrast, some *Deltaproteobacteria* produce intracellular greigite crystals (magnetosomes) under high H$_2$S concentrations (> 0.3 mM), but magnetite crystals under low H$_2$S conditions (< 0.3 mM) [50].

Spatially associated with the S$_8$ inclusions in MBav, we found the 1440 cm^{-1} Raman line (Fig. 2B), which most likely represents the CH$_2$ scissoring mode, which is usually pronounced in fatty acids (see Table 5, and [79–82]). Sulfur globules, however, have envelopes consisting solely of proteins, not lipids (see [83] for a review), at least in the case of *Proteobacteria*. For this member of the *Nitrospira*, we cannot determine characteristic Raman lines of specific amino acids (e.g. [73]) in the spectra containing the 1440 cm^{-1} line, yet the CH$_2$-related peak would be consistent with side chains of most proteinogenic amino acids.

The set of four lines 746, 1126, 1312 and 1586 cm^{-1} in our coccoid magnetic bacteria (Figure 5) matches the published

reference spectra of reduced cytochrome c [75,84,85], a heme-group-based perisplasmatic electron transporter involved in the respiratory chain of organisms. The heme group shows a series of strong Raman lines when probed with laser light in the wavelength range 500 nm to 530 nm [84], in which case the first electronic transition (Q transition) of porphyrin is excited so that resonant Raman (RR) scattering occurs. In the reduced state of cytochrome c (i.e., ferrous Fe), the pyrrole breathing mode v_{15} (752 cm^{-1}) is the most pronounced line ([75] and Table 5), which is also what we observe in the coccus (Figure 5). Cytochrome b and cytochrome c have similar RR spectra at 532 nm [86] and at 569 nm [87], but not at 515 nm [87], which would allow better discrimination between the two heme-proteins. A newly discovered family of c-type cytochrome referred to as magnetochrome, which has been exclusively found in magnetic bacteria [88], is likely to produce similarly strong RR lines as cytochrome c, due to similar UV-Vis absorption spectra. Magnetochrome, which as an iron oxidase controls the proper stoichiometry of magnetite [88], is probably incorporated in the magnetosome membrane, and therefore not periplasmatic as opposed to cytochrome c. Since the magnetosome chains in our bacteria are close to the cytoplasmic membrane [45], we cannot spatially separate signals from magnetochrome and cytochrome c. The presence of reduced cytochrome c, while exposing the cells to oxygen, suggests that cytochrome c has not transferred its electrons onto cytochrome c-oxidase, the terminal electron acceptor of the aerobic respiratory chain. This is probably due to a break down of the proton gradient during cell death while the sample was drying. From a more general perspective, cytochrome c occurs in the periplasmic

Table 2. Raman lines identified in our bacteria samples, and in synthetic reference samples.

MBav

Magnetite	S$_8$	S$_8$ crystalline	CH$_2$ fatty acids	Cytochrome C (II)
Fig. 3B,F	Fig. 3B,E	Fig. 3B,E	Fig. 3B,E	Fig. 3B,F
303s	151vs	800–950	1440m	750s
535m	219vs	(wide)		
665vs	467vs			

Vibrio / **Cocci**

Magnetite	Orthophosphate	Cytochrome C (II)	Magnetite	Cytochrome C (II)	Polyphosphate
Fig. 3A,F	Fig. 3A,E	Fig. 3F	Fig. 5A	Fig. 5B	Fig. 5A,B
303s	1080s	750s	193m	747vs	1177s
535s			303s	1126vs	
665vs			535s	1314vs	
			665vs	1586vs	

Synthetic greigite	Sodium thiosulfate		Sodium polyphosphate		Sodium phosphate	
Fig. 4	**		**		**	
253m	72s	448vs	221w	730sh	135w	532sh
327sh	93sh	533w	308sh	883w	226w	870vs
351vs	125s	556w	330m	950w	358m	922vs
367sh	150w	669vs	388sh	1008w	420m	998s
*	216w	1000vs	457w	1158vs	499m	1075w
	322s	1135s	511m	1261m	522sh	1175w
	360w	1155s	684s		541m	1288w

* Note the absence of lines at wavenumbers> 500 cm^{-1}.
** see also supplement Figures S1 to S3.
doi:10.1371/journal.pone.0107356.t002

Table 3. Candidate phosphorous compounds in bacterial inclusions (according to DoCampo [53]) and characteristic Raman lines for inorganic equivalents compiled from literature.

Pi	poly-P	Na-PPi	Ca-PPi
[69,70]	[64,65]	[66]	[67]
380m	700s	738w	353s
514m	1170vs	1122s	363sh
874s (sym. Stretch of P(OH)2)	2940m	1102w	440w
			486–620w (several)
940w			741sh
1075s (P = O stretch of PO2)			755s
			919w
1150w			1052vs
			1084w
			1117m
			1125m
			1186m

Pi = orthophosphate; poly-P = polyphosphate; PPi = pyrophosphate.
doi:10.1371/journal.pone.0107356.t003

Table 4. Characteristic Raman lines of sulfur allotropes, compiled from literature.

S$_6$	α-S$_7^*$	β-S$_7^*$	γ-S$_7^*$	δ-S$_7^*$	α-S$_8^*$	β-S$_8$
[61]	[61]	[61]	[61]	[61]	[97]	[61]
106w	145m	146m	143m	147w	150–161vs	151s
202s	150w	155s	151s	150w	182–199w	153s
262s	157s	182m	159w	155m	217–221vs	156s
448s	180m	185m	178s	185m	236–239w	195w
471vs	185m	239s	199w	201w	249–253m	217m
	239s	270m	237m	239s	419–420w	221vs
	241sh	285m	242vs	270w	434–442w	243w
	270m	358m	274m	285w	468–473m	249w
	285m	362s	285w	358m	472–474s	440m
	355s	395m	292w	363m	477–478vs	467m
	400s	400vs	364s	396m		272s
	420w	420w	400s	400vs		474s
	459m	459m	420w	419w	(polarization dependent shifts)	
	481vs	480vs	459m	460w		
	514m	511m	481s	480s		
	518s	518s	510m	510w		
	530w	528w	523w	518m		
				527w		

α-S$_9$	S$_{10}$	S$_6$S$_{10}$	S$_{11}^{**}$	S$_{12}^*$	S$_{13}^{*,**}$	S$_{14}^*$
[61]	[61]	[61]	[61]	[61]	[61]	[61]
100m	100m	103m	176s	127vs	100s	122w
104s	131m	136w	571vs	177/179m	135s	128s
111m	155w	145w		238/245m	175s	153m
117m	178m	172m		289m	205m	163m
151m	231w	201m		449s	280m	177w
155m	243m	207m		460vs	460vs	189w
161m	246sh	225w		475w		198m
181m	255w	228w				212w
188vs	403w	240m				234m
215m	425w	249w				243w
222m	466sh	265w				252w
245m	469s	272m				270w
256m	481sh	408w				444w
297m	487m	428m				447w
416w	495w	451m				453sh
436s		455sh				460s
442m		461sh				462sh
454vs		466m				468m
463m		479s				474wm
477m		489w				483w
485w						

endo-S$_{18}^*$	S$_{20}^*$	poly-S*,**	S$_8$	S$_{8,sol}$	S$_{8,cryst}$
[61]	[61]	[61]	[58]	[71]	[71]
130s	131vs	275w			114w
156m	248m	260w	154vs	152s	152s
165vs	267m	425w	188w	184w	184w
230s	464vs	460vs	220vs	218s	216s
450s			248w	248w	243w

Table 4. Cont.

465vs		299w	
476vs		334w	
	439w	437w	434m
	474vs	**475s**	**470s**
		591w	
			800–950
			(twophonon see [61])
		(in solution)	(crystalline)

* observed at 300 K or less;
** only the most prominent lines were taken from printed graphs (± 5 cm^{-1})
Raman line intensity: w = weak; m = medium; s = strong; vs = very strong; sh = shoulder of an adjoining line.

doi:10.1371/journal.pone.0107356.t004

space between the two lipid bilayer membranes in prokaryotes, e.g. in bacteria, or in eukaryotic cells, e.g. endosymbionts (mitochondria, chloroplasts). Therefore the Raman cytochrome signal defines the outlines of prokaryotes and it can be used to specifically map intact mitochondria and also to observe apoptotic cells that release cytochrome c into the cytosol [85]. For excitation of cytochrome, lasers tuned to the specific absorption of the heme group can be used at very low laser power to provide a sufficient signal from cytochromes due to RR scattering. This set up drastically reduces damage due to laser-induced heating and therefore is even suitable for examining living cells. This could be used to define for example the cell density on a surface or in a biofilm.

We have shown Raman microspectroscopy to be a powerful tool for the detection and mapping of intracellular sub-100 nm magnetite crystals, even though magnetite is a poor Raman scatterer and cells have a large autofluorescence background. The strength of Raman microscopy is the compound-specific filtering (by selecting the specific Raman lines) that allows one to detect and map objects with sizes below the optical detection limit. Using very low laser power, the excited volume can be kept small and the partial volume effect be maximized, which leads to a high spatial resolution in the wavenumber-filtered maps. With regard to magnetic biominerals, Raman spectroscopy is well suited to distinguish between magnetite and greigite without requiring electron microscopic investigations. Low laser power Raman spectroscopy is also highly suitable for detection and mapping of bacterial sulfur inclusions, where excess heat would cause chemical transformations and therefore experimental artifacts.

Materials and Methods

Magnetotactic bacteria were extracted from sediments that had been collected earlier from Lake Chiemsee (see [40] for sampling location and [89] for procedure). No permission was required for taking mud samples from Lake Chiemsee. The study does not involve endangered or protected species.

For purification, a drop of sediment is placed onto a microscope slide next to a drop of water. An external magnetic field is used to guide the magnetotactic bacteria from the sediment to the edge of the clear water drop, where the cells accumulate. For transmission electron microscopy (TEM) cells were pipetted off the drop, placed on a carbon coated copper grid and dried on air. For Raman microscopy and scanning electron microscopy (SEM) the cells were dried directly on the microscope slide. Cells were not

prepared with biological fixatives in order to avoid additional fluorescence, which reduces the efficiency of Raman detection of inorganic intracellular compounds. The preparation of the samples was done immediately before the Raman analysis.

Confocal Raman imaging was performed with an alpha 300R (WITec GmbH, Ulm, Germany). The excitation wavelength was 532 nm (2ω-Nd:YAG solid state laser). The laser power was adjusted to very low values (0.17 mW to 0.25 mW) in order to prevent oxidization of the magnetosomes from magnetite to hematite (e.g. [62,63,90–93]) and to preserve the molecular structure of sulfur [58]. A high numerical aperture (NA = 0.9, 100x) air objective was used in order to efficiently collect scattered light from the measurement spots.

For confocal imaging and compositional mapping, the core of a multimode fiber served as a pinhole with diameter 50 μm, leading to an axial resolution of $\sim$ 1 μm and a voxel volume of about 1 μm^3. The piezo-controlled scanning stage carrying the sample was stepped in intervals of 0.1μm in both x- and y-direction. At each confocal point, a Raman spectrum was acquired for 10 sec (10 acquisitions with 1 sec duration each), spanning the wavenumber range 0–3800 cm^{-1}, with a grating of 600 mm^{-1}. With the low laser power used, such long acquisition times are necessary to identify characteristic peaks of inorganic inclusions against the highly fluorescent background due to the organic material. The Rayleigh peak region (0–100 cm^{-1}) was strongly suppressed with a low-pass filter. The spectrometer was calibrated using a Si-wafer (520 cm^{-1}). Spikes due to cosmic rays were removed using the de-spiking option in the software. From characteristic Raman lines (and combinations thereof) identified in the measured spectra, we produced compositional maps showing the intensity of these lines at each pixel after background subtraction. On the basis of a threshold-intensity criterion, the intensity-encoded color brightness was adjusted such that only meaningful occurrences of a particular compound are depicted, while all non-meaningful occurrences remain black. Average spectra were obtained by first selecting a specific set of lines, and then by averaging the spectra over those regions that exclusively contain this set of lines. This way, the signal-to-noise ratio for the lines of interest can be enhanced.

An XploRA ONE confocal Raman microscope (Horiba Scientific, Kyoto, Japan), equipped with 532 nm, 638 nm, and 785 nm lasers, was used to acquire Raman point spectra on magnetic coccus bacteria (532 nm). It was also used to study excitation-wavelength dependence of Raman spectra in the sulfur

Table 5. Characteristic Raman lines of relevant organic compounds or functional groups (compiled from literature).

Cyto-chrome C (III)	Cyto-chrome C (II)	Fatty acids	Phospho-lipid	Fd	Ado	RPP
[75]	[75]	[73, 79–82]	[80, 99, 100]	[101]	[101]	[101]
757w	752vs	1063s*	715–746	282s	291s	290m
1125m	1128s	1130s*	plus fatty acid peaks	329sh	317w	313w
1170m	1173m	1300s**		339s	329w	336s
1315m	1313s	1440s***		367m	341sh	352sh
1561s	1489s			395m	349s	387s
1583m	1580s			426m	393w	578m
1635s	1617w			563w	421w	641m
				622w	581s	675m
				650sh	628sh	736m
				675m	641m	774m
				760w	683m	813m
				794w	741w	
					786m	
					814w	
					868w	

These can be observed also in eukaryotic cells (c.f. [85, 98]). Only the most prominent lines of fatty acids (or lipids) are listed. The defining phospholipid line is due to the symmetric diester O-P-O stretching mode of the polar head group and its precise wavenumber depends on various factors (see [100]); for the non-polar tail, see fatty acid lines in the column to the left.
Fd = Ferredoxin; Ado = Adrenodoxin; RPP = Red Paramagnetic Protein
*CH_2 bending/scissoring; **τ-(CH_2) twist; ***skeletal trans C–C stretch.
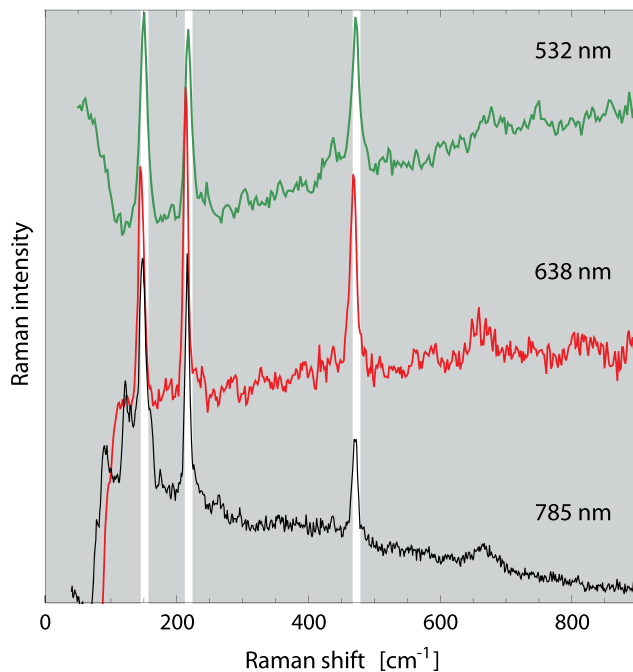doi:10.1371/journal.pone.0107356.t005

Figure 6. Raman spectrum of a sulfur inclusion in MBav, recorded at three different excitation wavelengths. The characteristic lines of S_8 (indicated by the white bars) appear consistently.
doi:10.1371/journal.pone.0107356.g006

inclusions of MBav, and to obtain the reference spectra of sodium thiosulfate (Sigma no. 72049), sodium polyphosphate (Riedel-de Haën no. 04267) and sodium phosphate (Sigma no. S8282).

For scanning-electron microscopy (performed after Raman analysis) with a JSM5900LV (JEOL, Japan), bacteria samples were plasma coated with a few atomic layers of gold. An acceleration voltage of 12 kV was chosen for SEM imaging. Elemental analysis was done by energy-dispersive X-ray (EDX) analysis at 12 kV (Röntec, Germany).

TEM micrographs of the separately prepared bacteria were taken with a JEM2011 (JEOL, Japan) operated at 120 kV.

In order to obtain a clean Raman reference spectrum for greigite, we hydrothermally synthesized greigite from iron(III)-chloride, thiourea, and formic acid, closely following the protocol by Tang et al. ([94]; see also [95]), and recorded with the low laser-power setup (0.2 mW, 532 nm) from a single greigite crystal with 10 accumulations over 5 sec integration time each. The Raman spectrum obtained (Figure 4) is characterized by a distinct line at 253 cm^{-1} and a broad band peaking at 351 cm^{-1} with shoulders at 327 and 367 cm^{-1}. This is consistent with the Raman spectrum obtained on a greigite powder sample with a 633 nm laser line and a 0.2 cm^{-1} grating [96]. Notable is the absence of lines above 500 cm^{-1}, which has not been reported in the literature yet. The dominant line for iron oxides which usually is around 660–670 cm^{-1} [63] is not present in the greigite spectrum. Since sulfur is heavier than oxygen, and the force constants for the bonds involving sulfur are smaller than those for oxygen, the vibration frequencies are lower. Lines of residual sulfur compounds from the synthesis or of possible greigite decomposition products were not detectable, which indicates the purity of the sample. The greigite lines (253 and 351 cm^{-1}) are right in between the characteristic

lines of magnetite (303 cm^{-1} and 535 cm^{-1}) and therefore the two minerals are well distinguishable in Raman spectroscopy. However, we found no evidence for greigite in the bacteria samples studied here.

Supporting Information

Figure S1   Raman spectra of sodium thiosulfate under three different excitation wavelengths.
(PDF)

Figure S2   Raman spectra of sodium phosphate under three different excitation wavelengths.
(PDF)

Figure S3   Raman spectra of sodium polyphosphate under three different excitation wavelengths.
(PDF)

Author Contributions

Conceived and designed the experiments: SE MW. Performed the experiments: SE AG. Analyzed the data: SE AG MW. Contributed to the writing of the manuscript: SE MW. Performed Scanning Electron microscopy and EDX: MH.

References

1. Frankel RB, Blakemore RP, Wolfe RS (1979) Magnetite in freshwater magnetotactic bacteria. Science 203: 1355–1356.
2. Torres de Araujo FF, Pires MA, Frankel RB, Bicudo CE (1986) Magnetite and magnetotaxis in algae. Biophys J 50: 376–378.
3. Bazylinski DA, Schlezinger DR, Howes BH, Frankel RB, Epstein SS (2000) Occurrence and distribution of diverse populations of magnetic protists in a chemically stratified coastal salt pond. Chem Geol 169: 319–318.
4. Lowenstam HA (1962) Magnetite in denticle capping in recent chitons (*Polyplacophora*). Bull Geol Soc Am 73: 435–438.
5. Walker MM, Kirschvink JL, Chang SB, Dizon AE (1984) A candidate magnetic sense organ in the yellow fin tuna, *Thunnus albacares*. Science 224: 751–753.
6. Eder SHK, Cadiou H, Muhamad A, McNaughton PA, Kirschvink JL, et al. (2012) Magnetic characterization of isolated candidate vertebrate magnetoreceptor cells. Proc Natl Acad Sci USA 109: 12022–12027.
7. Walcott C, Gould J, Kirschvink JL (1979) Pigeons have magnets. Science 205: 1027–1029.
8. Hanzlik M, Heunemann C, Holtkamp-Rötzler E, Winklhofer M, Petersen N, et al. (2000) Superparamagnetic magnetite in the upper beak tissue of homing pigeons. BioMetals 13: 325–331.
9. Komeili A (2012) Molecular mechanisms of compartmentalization and biomineralization in magnetotactic bacteria. FEMS Microbiol Rev 36: 232–255.
10. Faivre D, Schüler D (2008) Magnetotactic bacteria and magnetosomes. Chem Rev 108: 4875–4898.
11. Prozorov T, Bazylinski DA, Mallapragada SK, Prozorov R (2013) Novel magnetic nanomaterials inspired by magnetotactic bacteria: Topical review. Materials Science and Engineering: R: Reports 74: 133 – 172.
12. Kirschvink JL, Lowenstam HA (1979) Mineralization and magnetization of chiton teeth: Paleomagnetic, sedimentologic, and biological implications of organic magnetite. Earth Planet Sci Lett 44: 193–204.
13. Quintana C, Cowley JM, Marhic C (2004) Electron nanodiffraction and high-resolution electron microscopy studies of the structure and composition of physiological and pathological ferritin. J Struct Biol 147: 166–178.
14. Brem F, Hirt AM, Winklhofer M, Frei K, Yonekawa Y, et al. (2006) Magnetic iron compounds in the human brain: a comparison of tumour and hippocampal tissue. J R Soc Interface 3: 833–841.
15. Dunin-Borkowski RE, McCartney MR, Frankel RB, Bazylinski DA, Pósfai M, et al. (1998) Magnetic microstructure of magnetotactic bacteria by electron holography. Science 282: 1868–1870.
16. Lam KP, Hitchcock AP, Obst M, Lawrence JR, Swerhone GDW, et al. (2010) Characterizing magnetism of individual magnetosomes by X-ray magnetic circular dichroism in a scanning transmission X-ray microscope. Chem Geol 270: 110–116.
17. Kalirai SS, Lam KP, Bazylinski DA, Lins U, Hitchcock AP (2012) Examining the chemistry and magnetism of magnetotactic bacterium *Candidatus* Magnetovibrio blakemorei strain MV-1 using scanning transmission X-ray microscopy. Chem Geol 300–301: 14–23.
18. Kalirai SS, Bazylinski DA, Hitchcock AP (2013) Anomalous magnetic orientations of magnetosome chains in a magnetotactic bacterium: *Magnetovibrio blakemorei* strain MV-1. PLoS ONE 8: e53368. doi:10.1371/journal.pone.0053368.
19. Proksch RB, Moskowitz BM, Dahlberg ED, Schaeffer T, Bazylinski DA, et al. (1995) Magnetic force microscopy of the submicron magnetic assembly in a magnetotactic bacterium. Appl Phys Lett 66: 2582–2584.
20. Suzuki H, Tanaka T, Sasaki T, Nakamura N, Matsunaga T, et al. (1998) High-resolution magnetic force microscope images of a magnetic particle chain extracted from magnetic bacteria AMB-1. Jap J Appl Phys 37: 1343–1345.
21. Diebel CE, Proksch R, Green CR, Neilson P, Walker MM (2000) Magnetite defines a vertebrate magnetoreceptor. Nature 406: 299–302.
22. Körnig A, Hartmann MA, Teichert C, Fratzl P, Faivre D (2014) Magnetic force imaging of a chain of biogenic magnetite and monte carlo analysis of tip-particle interaction. J Phys D Appl Phys 47: 235403. doi:10.1088/0022-3727/47/23/235403.
23. Naresh M, Gopinadhan K, Sekhar S, Juneja P, Sharma M, et al. (2009) NSOM/HRTEM characterization of biologically derived cubo-octahedral nanomagnets. IEEE Trans Magn 45: 4861–4864.
24. Le Sage D, Arai K, Glenn DR, DeVience SJ, Pham LM, et al. (2013) Optical magnetic imaging of living cells. Nature 496: 486–489.
25. Lee AP, Webb J, Macey D, Van Bronswijk W, Savarese AR, et al. (1998) In situ Raman spectroscopic studies of the teeth of the chiton *Acanthopleura hirtosa*. J Biol Inorg Chem 3: 614–619.
26. Watanabe S, Yamanaka M, Sakai A, Sawada K, Iwasa T (2009) Laser Raman spectroscopic study of magnetite formation in magnetotactic bacteria. J Japan Inst Metals 73: 334–339.
27. Walker MM, Diebel CE, Haugh CV, Pankhurst PM, Montgomery JC (1997) Structure and function of the vertebrate magnetic sense. Nature 390: 371–376.
28. Lins U, Farina M (2004) Magnetosome chain arrangement and stability in magnetotactic cocci. Antonie van Leeuwenhoek 85: 335–341.
29. Farina M, Esquivel DMS, De Barros HGP (1990) Magnetic iron-sulphur crystals from a magnetotactic microorganism. Nature 343: 256–258.
30. Heywood B, Bazylinski D, Garratt-Reed A, Mann S, Frankel R (1990) Controlled biosynthesis of greigite (Fe_3S_4) in magnetotactic bacteria. Naturwissenschaften 77: 536–538.
31. Mann S, Sparks NHC, Frankel RB, Bazylinski DA, Jannasch HW (1990) Biomineralization of ferrimagnetic greigite (Fe_3S_4) and iron pyrite (FeS_2) in a magnetotactic bacterium. Nature 343: 258–261.
32. Bazylinski DA, Heywood BR, Mann S, Frankel RB (1993) Fe_3O_4 and Fe_3S_4 in a bacterium. Nature 366: 218.
33. Pósfai M, Buseck PR, Bazylinski DA, Frankel RB (1998) Iron sulfides from magnetotactic bacteria; structure, composition, and phase transitions. Am Mineral 83: 1469–1481.
34. Kasama T, Pósfai M, Chong RKK, Finlayson AP, Buseck PR, et al. (2006) Magnetic properties, microstructure, composition, and morphology of greigite nanocrystals in magnetotactic bacteria from electron holography and tomography. Am Mineral 91: 1216–1229.
35. Lins U, Keim CN, Evans FF, Farina M, Buseck PR (2007) Magnetite (Fe_3O_4) and greigite (Fe_3S_4) crystals in multicellular magnetotactic prokaryotes. Geomicrobiol J 24: 43–50.
36. Lefevre CT, Viloria N, Schmidt ML, Pósfai M, Frankel RB, et al. (2012) Novel magnetite-producing magnetotactic bacteria belonging to the gammaproteobacteria. ISME J: 440–450.
37. Wang Y, Lin W, Li J, Pan Y (2013) High diversity of magnetotactic *Deltaproteobacteria* in a freshwater niche. Appl Environ Microbiol 79: 2813–2817.
38. Wenter R, Wanner G, Schüler D, Overmann J (2009) Ultrastructure, tactic behaviour and potential for sulfate reduction of a novel multicellular magnetotactic prokaryote from north sea sediments. Environ Microbiol 11: 1493–1505.
39. Winklhofer M, Chang L, Eder SHK (2014) On the magnetocrystalline anisotropy of greigite (Fe_3S_4). Geochem Geophys Geosyst 15: 1558–1579.
40. Pan YX, Petersen N, Davila AF, Zhang LM, Winklhofer M, et al. (2005) The detection of bacterial magnetite in recent sediments of lake Chiemsee (southern Germany). Earth Planet Sci Lett 232: 109–123.
41. Lefevre CT, Trubitsyn D, Abreu F, Kolinko S, Jogler C, et al. (2013) Comparative genomic analysis of magnetotactic bacteria from the *Deltaproteobacteria* provides new insights into magnetite and greigite magnetosome genes required for magnetotaxis. Environ Microbiol 15: 2712–2735.
42. Pósfai M, Lefevre C, Trubitsyn D, Bazylinski DA, Frankel R (2013) Phylogenetic significance of composition and crystal morphology of magnetosome minerals. Frontiers Microbiol 4: 360–368.
43. Vali H, Förster O, Amarantidis G, Petersen N (1987) Magnetotactic bacteria and their magnetofossils in sediments. Earth Planet Sci Lett 86: 389–400.

44. Spring S, Amann R, Ludwig W, Schleifer KH, Van Gemerden H, et al. (1993) Dominating role of an unusual magnetotactic bacterium in the microaerobic zone of a freshwater sediment. Appl Env Microbiol 59: 2397–403.

45. Hanzlik M, Winklhofer M, Petersen N (1996) Spatial arrangement of chains of magnetosomes in magnetotactic bacteria. Earth Planet Sci Lett 145: 125–134.

46. Hanzlik M, Winklhofer M, Petersen N (2002) Pulsed-field-remanence measurements on indivdual magnetotactic bacteria. J Magn Magn Mater 248: 258–267.

47. Jogler C, Niebler M, Lin W, Kube M, Wanner G, et al. (2010) Cultivation-independent characterization of 'Candidatus magnetobacterium bavaricum' via ultrastructural, geochemical, ecological and metagenomic methods. Environ Microbiol 12: 2466–2478.

48. Jogler C, Wanner G, Kolinko S, Niebler N, Amann R, et al. (2011) Conservation of proteobacterial magnetosome genes and structures in an uncultivated member of the deep-branching Nitrospira phylum. Proc Natl Acad Sci USA 108: 1134–1139.

49. Li J, Pan Y, Liu Q, Yu-Zhang K, Menguy N, et al. (2010) Biomineralization, crystallography and magnetic properties of bulletshaped magnetite magnetosomes in giant rod magnetotactic bacteria. Earth Planet Sci Lett 293: 368–376.

50. Lefevre CT, Frankel RB, Abreu F, Lins U, Bazylinski DA (2011) Culture-independent characterization of a novel uncultivated magnetotactic member of the Nitrospirae phylum. Environ Microbiol 13: 538–549.

51. Lin W, Li J, Pan Y (2012) Newly isolated but uncultivated magnetotactic bacterium of the phylum Nitrospirae from Beijing, China. Appl Environ Microbiol 78: 668–675.

52. Keim CN, Solorzano G, Farina M, Lins U (2005) Intracellular inclusions of uncultured magnetotactic bacteria. Int Microbiol 8: 111–117.

53. Docampo R (2006) Acidocalcisomes and polyphosphate granule. In: Shively J, editor, Inclusions in Prokaryotes, Berlin: Springer. pp. 53–70.

54. Pickering IJ, George GN, Yu EY, Brune DC, Tuschak C, et al. (2001) Analysis of sulfur biochemistry of sulfur bacteria using X-ray absorption spectroscopy. Biochem 40: 8138–8145.

55. Prange A, Chauvistre R, Modrow H, Hormes J, Trueper HG, et al. (2002) Quantitative speciation of sulfur in bacterial sulfur globules: X-ray absorption spectroscopy reveals at least three different species of sulfur. Microbiol 148: 267–276.

56. Lee YJ, Prange A, Lichtenberg H, Rohde M, Dashti M, et al. (2007) In situ analysis of sulfur species in sulfur globules produced from thiosulfate by Thermoanaerobacter sulfurigignens and Thermoanaerobacterium thermosulfurigenes. J Bacteriol 189: 7525–7529.

57. George GN, Gnida M, Bazylinski DA, Prince RC, Pickering IJ (2008) X-ray absorption spectroscopy as a probe of microbial sulfur biochemistry: the nature of bacterial sulfur globules revisited. J Bacteriol 190: 6376–6383.

58. Pasteris J, Freeman JJ, Goffredi SK, Buck KR (2001) Raman spectroscopic and laser scanning confocal microscopic analysis of sulfur in living sulfur-precipitating marine bacteria. Chem Geol 180: 3–18.

59. Himmel D, Maurin LC, Gros O, Mansot JL (2009) Raman microspectrometry sulfur detection and characterization in the marine ectosymbiotic nematode Eubostrichus dianae (Desmodoridae Stilbonematidae). Biol Cell 101: 43–54.

60. Dahl C, Prange A (2006) Bacterial sulfur globules: Occurrence, structure and metabolism. In: Shively J, editor, Inclusions in Prokaryotes, Microbiology Monographs, Berlin: Springer. pp. 21–51. doi:10.1007/3-540-33774-1-2.

61. Eckert B, Steudel R (2003) Molecular spectra of sulfur molecules and solid sulfur allotropes. Top Curr Chem 231: 31–98.

62. Shebanova ON, Lazor P (2003) Raman spectroscopic study of magnetite (Fe_3O_4): a new assignment for the vibrational spectrum. J Sol State Chem 174: 424–430.

63. Shebanova ON, Lazor P (2003) Raman study of magnetite (Fe_3O_4): laser-induced thermal effects and oxidation. J Raman Spectrosc 34: 845–852.

64. de Jager HJ, Heyns AM (1998) Kinetics of acid-catalyzed hydrolysis of a polyphosphate in water. J Phys Chem A 102: 838–2841.

65. Majed N, Gu AZ (2010) Application of Raman microscopy for simultaneous and quantitative evaluation of multiple intracellular polymers dynamics functionally relevant to enhanced biological phosphorus removal processes. Environ Sci Technol 44: 8601–8608.

66. Majed N, Matthäus C, Diem M, Gu AZ (2009) Evaluation of intracellular polyphosphate dynamics in enhanced biological phosphorus removal process using Raman microscopy. Environ Sci Technol 43: 5436–5342.

67. Cornilsen BC (1984) Solid state vibrational spectra of calcium pyrophosphate dihydrate. J Mol Struct 117: 1–9.

68. Chen SC, Kuo PC, Hsu SL, Lin GP, Ou SL, et al. (2009) Granular Co_3Pt thin films with perpendicular hard magnetic properties for perpendicular magnetic recording media. IEEE Trans Magn 45: 2280–2283.

69. Preston CM, Adams WA (1979) A laser Raman spectroscopic study of aqueous orthophosphate salts. J Phys Chem 83: 814–821.

70. Okabayashi H, Yoshida T, Ikeda T, Matsuura H, Kitagawa T (1982) Metaphosphite (PO_2^-) symmetric-stretching raman line and molecular-aggregation states of barium dialkyl phosphates. J Am Chem Soc 104: 5399–5402.

71. Scott DW, McCullough J, Kruse F (1964) Vibrational assignment and force constants of S_8 from a normal-coordinate treatment. J Mol Spectrosc 13: 313–320.

72. Williams A, Edwards H (1994) Raman spectra of human keratotic biopolymers: skin, callus, hair and nail. J Raman Spectrosc 25: 95–98.

73. de Gelder J, de Gussem K, Vandenabeele P, Moens L (2007) Reference database of Raman spectra of biological molecules. J Raman Spectrosc 38: 1133–1147.

74. Wang A, Haskin LA, Jolliff BL (1998) Characterization of mineral products of oxidation and hydration by laser raman spectroscopy – Implications for in situ petrologic investigation on the surface of Mars. 29th Annual Lunar and Planetary Science Conference, March 16–20 1998, Houston, TX, abstract no 1819.

75. Adar F (1978) Resonance Raman spectra of ferric cytochrome c. A probe of low-lying electronic levels of the iron ion. J Phys Chem 82: 230–234.

76. Bazylinski DA, Dean AJ, Williams TJ, Long LK, Middleton SL, et al. (2004) Chemolithoautotrophy in the marine, magnetotactic bacterial strains MV-1 and MV-2. Arch Microbiol 182: 373–387.

77. Garrels RM, Christ CL (1965) Solutions, Minerals, and Equilibria. New York, USA: Harper and Row.

78. Rickard D, Luther GW (2007) Chemistry of iron sulfides. Chem Rev 107: 514–562.

79. Schachtschneider JH, Snyder RG (1963) Vibrational analysis of the n-parafines - ii normal co-ordinate calculations. Spectrochim Acta A 19: 117–168.

80. Gaber BP, Yager P, Peticolas WL (1978) Deuterated phospholipids as nonperturbing components for Raman studies of biomembranes. Biophys J 22: 191–207.

81. Wong PTT (1984) Raman spectroscopy of thermotropic and high-pressure phases of aqueous phospholipid dispersions. Ann Rev Biophys Bioeng 13: 1–24.

82. Frank CJ, McCreery RL, Redd DCB (1995) Raman spectroscopy of normal and diseased human breast tissues. Anal Chem 67: 777–783.

83. Maki JS (2013) Bacterial intracellular sulfur globules: structure and function. J Mol Microbiol Biotech 23: 270–280.

84. Spiro TG, Streaks TC (1972) Resonance Raman spectra of hemoglobin and cytochrome c: Inverse polarization and vibronic scattering. Proc Nat Acad Sci USA 69: 2622–2626.

85. Okada M, Smith NI, Palonpon AF, Endo H, Kawata S, et al. (2012) Label-free raman observation of cytochrome c dynamics during apoptosis. Proc Nat Acad Sci USA 101: 28–32.

86. Ogawa M, Harada Y, Yamaoka Y, Fujita K, Yaku H, et al. (2009) Label-free biochemical imaging of heart tissue with high-speed spontaneous Raman microscopy. Biochem Biophys Res Comm 382: 370–374.

87. Adar F, Erecinska M (1974) Resonance Raman spectra of the b- and c-type cytochromes of succinate cytochrome c reductase. Arch Biochem Biophys 165: 570–580.

88. Siponen MI, Legrand P, Widdrat M, Jones SR, Zhang WJ, et al. (2013) Structural insight into magnetochrome-mediated magnetite biomineralization. Nature 502: 681–684.

89. Mao X, Egli R, Petersen N, Hanzlik M, Liu X (2014) Magneto-chemotaxis in sediment: First insights. PLoS ONE 9: e102810. doi:10.1371/journal.pone.0102810.

90. de Faria DLA, Vena S (1997) Raman microspectroscopy of some iron oxides and oxyhydroxides. J Raman Spectrosc 28: 873–878.

91. Hanesch M (2009) Raman spectroscopy of iron oxides and (oxy)hydroxides at low laser power and possible applications in environmental magnetic studies. Geophys J Int 177: 941–948.

92. Lübbe M, Gigler AM, Stark RW, Moritz W (2010) Identification of iron oxide phases in thin films grown on Al_2O_3 (0001) by Raman spectroscopy and X-ray diffraction. Surf Sci 604: 679–685.

93. Li YS, Church JS, Woodhead AL (2012) Infrared and Raman spectroscopic studies on iron oxide magnetic nano-particles and their surface modifications. J Magn Magn Mater 324: 1543–1550.

94. Tang Y, Chen QW, Xiong Y, Li Y (2007) Magnetic field-induced increase in conversion rate of Fe_3S_4 to FeS_2. Chin J Inorg Chem 23: 941–947.

95. Chang L, Roberts AP, Muxworthy AR, Tang Y, Chen Q, et al. (2007) Magnetic characteristics of synthetic pseudo-single-domain and multi-domain greigite (Fe_3S_4). Geophys Res Lett 34: 1–6.

96. Bourdoiseau JA, Jeannin M, Remazeilles C, Sabot R, Refait P (2011) The transformation of mackinawite into greigite studied by Raman spectroscopy. J Raman Spectrosc 42: 496–504.

97. Gautier G, Debeau M (1973) Spectres di vibration d'un monocristal de soufre orthorhombique. Spectrochim Acta 80: 1193–1198.

98. Klein K, Gigler AM, Aschenbrenner T, Monetti R, Bunk W, et al. (2012) Label-free live-cell imaging with confocal Raman microscopy. Biophys J 102: 360–368.

99. Bulkin BJ, Krishnamachari N (1972) Vibrational spectra of liquid crystals iv. Infrared and Raman spectra of phospholipid-water mixtures. J Am Chem Soc 94: 1109–1112.

100. Bicknell-Brown E, Brown KG, Person WB (1982) Conformation-dependent Raman bands of phospholipids surfaces: 3 - Head group ortho-phosphate stretching vibrations. J Raman Spectrosc 12: 180–189.

101. Han S, Czernuszewicz RS, Kimura T, Adam MWW, Spiro TG (1989) Fe_2S_2 protein resonance Raman spectra revisited: structural variations among adrenodoxin, ferredoxin, and red paramagnetic protein. J Am Chem Soc 111: 3505–3511.